Stochastic Simulation Model for the 3D Morphology of Composite Materials in Li-Ion Batteries

Ralf Thiedmann[1] Ole Stenzel[1] Aaron Spettl[1] Paul R. Shearing[2]
Stephen J. Harris[3] Nigel P. Brandon[2] Volker Schmidt[1]

August 30, 2010

Abstract

Battery technology plays an important role in energy storage. In particular, lithium–ion (Li-ion) batteries are of great interest, because of their high capacity, long cycle life, and high energy and power density. However, for further improvements of Li-ion batteries, a deeper understanding of physical processes occurring within this type of battery, including transport, is needed. To provide a detailed description of these phenomena, a 3D representation is required for the morphology of composite materials used in Li-ion batteries. In this paper, we develop a stochastic simulation model in 3D, which is based on random marked point processes, to reconstruct real and generate virtual morphologies. For this purpose, a statistical technique to fit the model to 3D image data gained by X-ray tomography is developed. Finally, we validate the model by comparing real and simulated data using image characteristics which are especially relevant with respect to transport properties.

Keywords : Lithium-Ion Batteries, 3D Imaging, Stochastic Simulation Model, Structural Analysis, Marked Point Process, Germ-Grain Model, Model Fitting, Model Validation

[1] Ulm University, Institute of Stochastics, D-89069 Ulm, Germany
[2] Imperial College, Department of Earth Science & Engineering, London SW7 2AZ, UK
[3] General Motors, R&D Center Electro-Chemistry and Battery Systems, Warren, MI 48090-9055, USA

1 Introduction

Batteries are a very important and already well–engineered technology. However, not all physical phenomena within batteries are well understood so far. Most models for transport processes only take global parameters into account, so that the detailed 3D morphology of the media within which the transport processes of lithium ions are occurring is not considered, see Verbrugge and Koch (2003). One reason for this is the fact that imaging of the 3D morphology in high resolution is a difficult task. The first 3D images of both positive and negative composite electrodes used in Li-ion batteries have been obtained very recently, see e.g. Shearing *et al.* (2010) and Wilson *et al.* (2010). They allow a deeper insight into the interior of this type of batteries. Hence, in Shearing *et al.* (2010), a first descriptive analysis of the 3D structure of Li-ion batteries has been performed with respect to transport-relevant properties, where the lithium–transporting phase is interpreted as a 'pore phase' and the graphite as a 'solid phase'. We will use this terminology in the present paper as well.

Here, we go one step further than simply analyzing the 3D morphology in a purely descriptive way by developing a stochastic simulation model for the pore phase based on the above mentioned 3D image data of Li-ion batteries, see Figure 1. More precisely, the model, which we propose in the present paper, is based on tools from stochastic geometry, especially on point–process models. Hence, for image segmentation, we use an algorithmic approach described in Stenzel *et al.* (2010) to come up with a suitable representation of the pore phase by unions of overlapping spheres. It can be seen as a realization of a random marked point process, where the centers of spheres are the points and the corresponding radii are the marks. See also Yi et al. (2004) and Yi et al. (2006) where unions of overlapping ellipsoids have been

considered for structural analyses of Li-ion electrode materials.

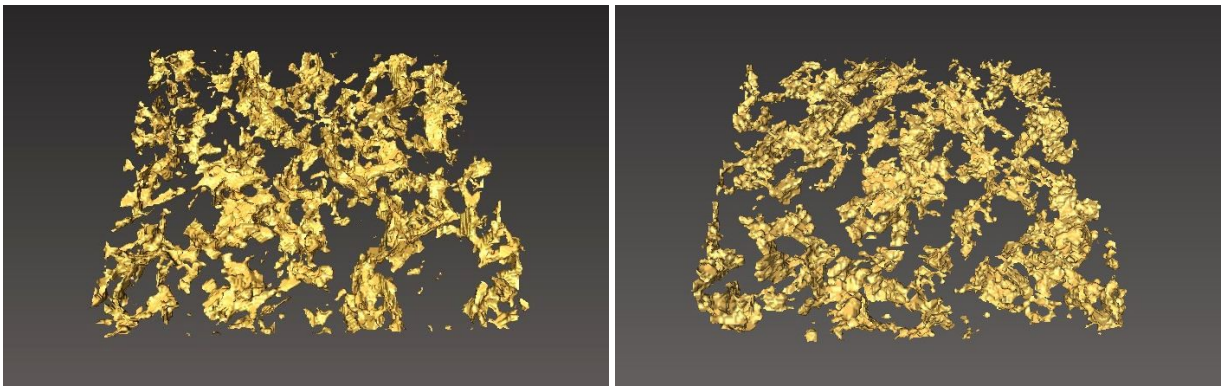

Figure 1: Left: 3D cutout of original data from Li-ion batteries; right: 3D cutout of a realization of the stochastic simulation model

In addition to our model itself, we present a method of spatial statistics to estimate the model parameters, i.e., to fit our model to the data obtained in Shearing *et al.* (2010) by means of X-ray tomography. For validating the fitted model, we consider structural image characteristics which describe transport-relevant properties, and compare them for simulated data obtained from the model and for real data, respectively. Comprehensive surveys on recent results in the fields of stochastic geometry and spatial statistics can be found in Kendall and Molchanov (2010) and Gelfand *et al.* (2010).

In a next step of investigating Li-ion batteries and especially the transport processes therein, which will be discussed in a forthcoming paper, the proposed model will be used to generate virtual structures for the 3D morphology of Li-ion batteries. Such a computer-based approach allows us to analyze the influence of morphology on the performance of batteries. Thus, our stochastic simulation model can be used for virtual material design based on computer experiments, i.e., to predict and construct morphologies of Li-ion batteries that are optimal w.r.t. transport. This kind of analysis can help to reduce expensive and time–consuming physical experiments and measurements. Note that the fitting of the model to real data and its subsequent validation are necessary pre-conditions for virtual material design. In

this sense the fitting is an adjustment of the model, and the validation shows whether the morphological structure observed in real data can be reconstructed by the model sufficiently well.

In these porous materials, there are inherent statistical deviations in microstructure; these deviations must be compensated for by characterizing sufficiently large volumes to be representative of the bulk microstructure. The ability to accurately reproduce microstructures derived from high-resolution tomography experiments can enable large-scale replication of electrode analogues in silica. This may be especially useful for simulation of transport phenomena in porous materials, which often requires some microstructural framework.

The paper is organized as follows. In Section 2 the real 3D data, their exploration and preprocessing is briefly described. Then in Section 3 a stochastic segmentation algorithm is considered to find a suitable representation of the pore space by unions of overlapping spheres. In Section 4 the modeling approach including a technique for model fitting is explained, whereas Section 5 deals with the validation of the stochastic simulation model by means of structural image characteristics. Finally, in Section 6 a brief summary and an outlook to possible future research using the stochastic simulation model is given.

2 3D Images of Li-Ion Batteries

This paper deals with 3D images of composite materials used in Li-ion batteries, which have been obtained by X-ray tomography as described in Shearing *et al.* (2010). These images allow, for the first time, a detailed investigation of the inner 3D structure of Li-ion batteries. To begin with, we give a short description of the imaging techniques, the images themselves, and the methods for image segmentation which have been applied in this context.

2.1 Experimental

Tomography studies have been performed on the graphite composite electrode from a commercial Lishen 2.2 Ah 18650 laptop cell. The battery was completely discharged and then opened, and the graphite electrode was harvested. The graphite electrode of the working cell is bonded to a Cu current collector. In order to facilitate X-ray tomography studies, the Cu layer was removed by dissolution in nitric acid — this dissolution process is also expected to remove any residual electrolyte material. EDS and SEM images of the electrode composite show (see Harris *et al.* (2010)) that the graphite particles are typically 10 to 15 microns in diameter. Since the electrode is only about 60 microns thick, the electrode is unlikely to be structurally homogeneous, but inherent statistical deviations in microstructure can occur.

An area of the isolated graphite electrode layer was subsequently identified and mounted on a pin for analysis by X-ray tomography. The SEM hosted Gatan X-ray ultramicroscope (XuM) system was used for high resolution computerized tomography (nano-CT). Projected X-ray images were acquired at 1° rotation increments over 190° and reconstructed using Gatan's cone–beam back–projection algorithm to generate a 3D volume. The images were acquired with an 80 s exposure time (total acquisition time of 4.2 h) and a total magnification of $41.4\times$, corresponding to 480 nm voxel dimensions. The reconstructed gray–scale tomography data was analyzed using the Avizo software package (Mercury computer systems, 2008): the raw data was filtered using the 'Edge Preserving Smoothing Tool' (also known as anisotropic diffusion – see e.g. Weikert (1998)) before binarization by global thresholding.

The considered data set for composite graphite electrodes used in Li-ion batteries has a size of $750 \times 499 \times 89$ voxels, where each voxel has a size of $(480nm)^3$, see Figure 1 (left). This is a cutout of the complete 3D data set which is chosen to avoid edge effects. Note that all parameter values in the present paper are given in voxels, where we will regard the lithium–

transporting phase as 'pore space' considering it as (black) foreground phase, and the solid as the (white) background phase, see Figure 2. To fix notation, let B be the pore phase of the binarized data set, and B^c its complement, i.e., the solid phase.

Figure 2: Cutout of a 2D slice of composite materials in Li-ion batteries

2.2 Morphological Smoothing

To come up with a sufficiently simple mathematical model for the pore space, we apply a preliminary smoothing of the pore phase by some morphological operations, especially by using a so–called dilation, see e.g. Jähne (2005) for more details on this type of image transformations and their applications in image analysis. Note that a dilation can be imagined as a 'blowing up' of the considered phase. More formally, for any fixed dimension $d \geq 1$, the dilation of a set $A \subset \mathbb{R}^d$ by a set $C \subset \mathbb{R}^d$, where C is called a structuring element, is defined by

$$A \oplus C = \{a + c : a \in A, c \in C\}\,.$$

In the present paper, dilations are considered where the structuring element C is a set of the form $b(o, r) = \{x \in \mathbb{R}^d : |x| \leq r\}$, i.e., a sphere around the origin o with some radius $r > 0$. In particular, the pore phase $B \subset \mathbb{R}^3$ is transformed as follows. To remove small

'pores' in the solid phase, which can be seen as artifacts caused e.g. by the imaging itself or the binarization, we apply a dilation of the solid phase B^c and a subsequent dilation of the 'reduced' pore phase $(B^c \oplus b(o,r))^c$ using the same dilation radius $r = \sqrt{3}$ in both cases. The result $B' = (B^c \oplus b(o,r))^c \oplus b(o,r)$ of this combined transformation is called an opening of the pore phase B. It removes (very) small parts of the pore phase located in predominantly solid regions. This operation can be seen as a morphological smoothing of the solid phase.

Since our modeling approach will be based on a representation of the pore phase B by unions of overlapping spheres, a further smoothing of the boundary of B' is required. This can be achieved by an additional dilation of the (already opened) pore phase B' using the sphere $b(o,1)$ as structuring element.

The final result of these morphological operations on B is a smoothed set denoted by B'', i.e.,

$$B'' = B' \oplus b(o,1) = \left(B^c \oplus b(o,\sqrt{3})\right)^c \oplus b(o,1+\sqrt{3})\,,$$

which is more suitable to be represented by unions of overlapping spheres, see also Stenzel *et al.* (2010). We will then model the smoothed pore phase B'' by a union of random spheres with random centers and random radii, see Section 4 below.

To summarize, the smoothing of the pore phase is done for two reasons. First, it removes artifacts, i.e., very small pore–particles within the solid phase, which can result from imaging or binarization, but do not appear in real materials. Since hardly any Li+ ion transport occurs in the smallest pores, it may not be a problem if their shape, size, and number are not perfectly modeled. On the other hand, the boundary of the pore phase gets smoother which provides the opportunity of stochastic modeling of the pore phase by unions of random (overlapping) spheres.

Note, however, that we do not neglect those parts of the original pore phase B which have

been removed by the morphological transformations and influence the physical properties of the composite material. These parts are included into the model later on, after modeling the smoothed pore phase B'', see Section 4.3.

3 Representation by Unions of Overlapping Spheres

In this section, we explain how a suitable representation of the smoothed pore phase B'' by unions of overlapping spheres can be constructed, where we use a slightly modified version of the stochastic segmentation algorithm considered in Stenzel *et al.* (2010). In Figure 3 a (schematic) illustration of such a representation is shown in 2D, but note that the actual method is implemented in 3D.

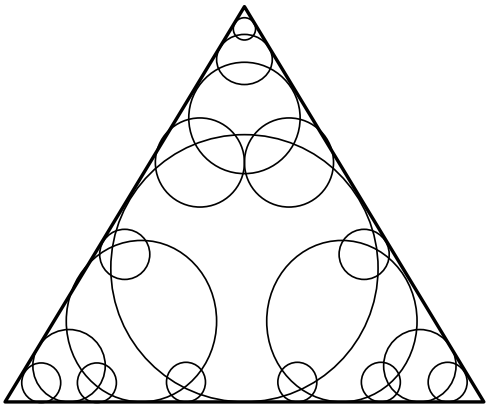

Figure 3: Schematic 2D example of the representation by unions of spheres

The basic idea is to find preferred locations of centers of the spheres by means of a so–called intensity map. Thus the main steps of our segmentation algorithm can be described as follows:

0) An 'empty' intensity map for preferred locations of centers is generated.

1) Put a point s at random into the set B'' and mark it with the maximum radius $r_{\max}$

such that the sphere $b(s, r_{\max}) = \{x \in \mathbb{R}^3 : |x - s| \leq r_{max}\}$ is completely contained in B''. Then, a candidate for the next center of a sphere is located at random in B''. A candidate $s' \in B''$ is rejected if the sphere $b(s', r'_{\max})$ centered at this point is completely covered by other spheres which have been put (and accepted) earlier. This process of 'sphere placement' is continued until a certain desired volume fraction of B'', say 99%, is covered.

2) The centers of spheres found in step 1) are added to the intensity map using kernel density estimation with adaptive bandwidths.

3) Repeat steps 1) and 2) several times to get an average of preferred locations of centers.

4) The local maxima of the resulting intensity map, which show preferred locations of centers, are used in order to construct the final representation of B'' by unions of spheres.

In the following, this stochastic segmentation algorithm is explained in detail.

3.1 Sphere–Placement Algorithm

A point s is located at random in the set B'', i.e., it follows the principle of complete spatial randomness, and marked with the maximum radius $r_{\max}$ of a sphere $b(s, r_{\max})$ which is completely contained in B''. The computation of the maximum radius $r_{\max}$ can be done very efficiently applying a distance transformation to B'', see e.g. Saito and Toriwaki (1994). The location of s is accepted if the radius $r_{\max}$ is at least $\sqrt{3}$, to avoid spheres only representing one single voxel, and if the sphere is not completely covered by other spheres which have been put (and accepted) earlier. This process of sphere placement is continued until a certain volume fraction of B'', say 99%, is covered by spheres.

3.2 Intensity Map

To get an average over several runs of sphere placement, the preferred locations of centers are determined using an intensity map. Such a map is constructed using kernel density estimation (see e.g. Scott (1992) for details) for the locations of centers obtained by the above described sphere–placement algorithm. Hence each complete run of sphere placement is seen as one sample, i.e., the locations of the centers of each run are included into the intensity map using kernel density estimation. Note that the main problem of kernel density estimation is the right choice of bandwidth. If the bandwidth is too small, the image is over–segmented, i.e., the intensity map has too many local maxima and, consequently, too many centers are generated. On the other hand, if the bandwidth is too large, only a few local maxima and centers, respectively, are obtained. To solve this problem, we choose an adaptive procedure for bandwidth selection. Hence, several intensity maps can be generated for different bandwidths. For the first time of generating the intensity map, the bandwidth is set equal to a large value, then kernel density estimation for all realizations of the sphere–placement algorithm is executed. All local maxima of the intensity map obtained in this way are assumed to be potential centers of spheres. If the union of resulting spheres does not cover a sufficiently large fraction of B'', missing spheres are added by applying the same method but with a smaller bandwidth. To avoid an over-segmentation not all local maxima are chosen to belong to the final set of sphere-centers. More precisely, the procedure is as follows. Around each potential sphere–center, i.e., local maxima of the intensity map, a sphere is drawn, where its radius is the largest radius that the sphere is still completely contained in B''. The largest sphere obtained in this way is put to the final union of spheres. All other spheres are ordered descendingly with respect to that part of their volume which is not yet covered by other spheres already accepted for the final union of spheres. Then the first sphere of this list is put to the final union of spheres and a new ordering is done. This

procedure is repeated until either the required volume fraction of B'' is covered by the union of spheres, or no local maximum is left.

Note that for a bandwidth being too large, a too small fraction of volume of the set B'' is covered. So we repeat the kernel density estimation using a smaller bandwidth and choose again the local maxima to be added to the set of preferred centers. The bandwidth is decreased until 99% of the total volume of B'' is covered. Note that only such spheres are added to the list of preferred spheres which are not totally covered by other, already accepted spheres. The resulting union of all spheres is then a representation of B''. It will be denoted by B'''.

For improving the accuracy of our segmentation procedure, i.e., to increase the number of local maxima in the intensity map, we have increased the resolution of the intensity map w.r.t. the original data. More precisely, each voxel of the original data set is represented by 8 voxels in the intensity map.

3.3 Representation as Marked Point Pattern

The representation B''' of the smoothed pore phase B'' by unions of overlapping spheres can be seen as functional of a marked point pattern $(s_1, r_1), \ldots, (s_n, r_n)$, where the points s_i are the locations of the centers of spheres and the marks r_i are the corresponding radii. In other words, it holds

$$B''' = \bigcup_{i=1}^{n} b(s_i, r_i)\,.$$

In the following, we will model this union of spheres by a random marked point process using tools from stochastic geometry.

4 Germ–Grain Model

The representation of the smoothed pore phase B'' by unions of spheres, which has been constructed in Section 3, can be interpreted as a realization of a marked point process, where the points describe the locations and the marks the radii of the corresponding spheres. This kind of a random marked point process is called a germ–grain model in stochastic geometry, see e.g. Daley and Vere-Jones (2003/07), Diggle (2003), Illian *et al.* (2008), Kendall and Molchanov (2010), and Stoyan *et al.* (1995) for further details.

The construction of such marked point processes can be decomposed into two main steps. The first step is to model the points (germs) separately from the marks, see Section 4.1. The marks (grains) are then added to a given realization of the (unmarked) point process of germs which is described in Section 4.2.

4.1 Modeling of Germs

4.1.1 Elliptical Matérn Cluster Point Processes

For modeling the centers s_i of spheres, we choose a 3D Matérn cluster point process $\{S_i\}$, where the clusters have an elliptical shape. This model has two different components. In a first step, so–called parent points are generated which form a stationary Poisson point process, i.e., the number of (parent) points in any sampling window $W \subset \mathbb{R}^3$ follows a Poisson distribution whose parameter is proportional to the volume $|W|$ of W. This means that the expected number of parent points in W is given by $\lambda_p|W|$ for some constant $\lambda_p > 0$ which is called the intensity of the Poisson process. The locations of these points follow the principle of complete spatial randomness, i.e., they are (conditionally) uniformly distributed in W.

In a second step, so–called child points are generated around each parent point, within an ellipsoid centered at the parent point. These child points also form stationary Poisson point processes, but restricted to their ellipsoids. The ellipsoids and the child points therein are subsequently rotated uniformly around their centers. In the final model, only the union of all child points is considered which form a stationary and isotropic point process in $\mathbb{R}^3$, i.e., its distribution is invariant under shifts and rotations around the origin.

The parameters of the Matérn cluster point process with elliptical clusters are the intensity λ_p of the parent point process, the mean number c of child points per cluster, and the lengths l_1, l_2, and l_3 of the three axes describing the ellipsoids, where we have found out that the assumption that $l_1 = l_2$ is in accordance with the data analyzed in the present paper.

4.1.2 Model Fitting

For fitting the Matérn cluster point process to our data, we apply the method of minimum–contrast estimation which is very common in spatial statistics, see e.g. Illian *et al.* (2008). The idea of this method is to minimize the discrepancy between a characteristic which is computed for the model depending on its parameters, and the same characteristic estimated from real data. Then the solution of this minimization problem is called a minimum–contrast estimator for the model parameters.

In our case, we have chosen to use the so–called pair-correlation function $g(r)$ for model fitting, because this second–order characteristic contains comprehensive structural information. A detailed description of this characteristic is postponed to Appendix A. In the present section, only a short overview is given on how to use the pair-correlation function for model fitting.

Note that for the considered class of Matérn cluster point processes with elliptical clusters, the pair-correlation function $g_\theta(r)$ depends on the parameter vector $\theta = (\lambda_p, l_1, l_3)$. Analytical

formulae for $g_\theta(r)$ can be found in Appendix A.

The minimum–contrast method leads to the following estimator $\widehat{\theta} = (\widehat{\lambda}_p, \widehat{l}_1, \widehat{l}_3)$ for θ:

$$\widehat{\theta} = \text{argmin}_\theta \int_{r_1}^{r_2} (g_\theta(r) - \widehat{g}(r))^2 \mathrm{d}r \,,$$

where $\widehat{g}(r)$ is the empirical pair-correlation function which is computed from real data. The restriction of the domain of integration in the above formula to some interval $[r_1, r_2]$ with $r_2 > r_1 > 0$ is reasonable, because the computation of the estimator $\widehat{g}(r)$ for small $r > 0$ is not stable and for very large r the values of $\widehat{g}(r)$ are not relevant for structural analyses.

To determine the mean number c of child points per cluster, we use the relationship

$$c = \frac{\lambda}{\lambda_p} \,,$$

where λ is the total intensity of the Matérn cluster process, which can be computed by the natural estimator $\widehat{\lambda}$ being the ratio of the number of points in some sampling window W divided by the volume of W. We then put $\widehat{c} = \widehat{\lambda} / \widehat{\lambda}_p$.

The results for fitting the Matérn cluster point process to the pattern of sphere–centers considered in Section 3.3 are given as $\widehat{\lambda}_p = 0.00015$, $\widehat{c} = 33.33$, $\widehat{l}_1 = \widehat{l}_2 = 22.2$, and $\widehat{l}_3 = 3$.

4.1.3 Model Validation

To validate the model which has been obtained in the previous section, we consider so–called summary characteristics from point–process statistics, e.g. the nearest–neighbor distance distribution, the spherical contact distribution, the L-function, and the pair-correlation function. Note however that the pair-correlation function has already been used to fit the model to data, i.e., it should be rather similar for real and simulated data, respectively. In the following, only an intuitive description of the considered characteristics is given. Formal definitions can be found e.g. in Illian *et al.* (2008) and Stoyan *et al.* (1995).

Using summary characteristics for model validation, we want to find out whether the point pattern of sphere centers extracted from real data can be seen as a realization of the fitted model. Thus, to check whether the model fits sufficiently well to real data, we compute pointwise 96% confidence intervals for several summary characteristics, based on simulated data. The model can be seen as well fitting with respect to the considered characteristic if the values of this characteristic, estimated from real data, are within (or close to) these confidence intervals.

The idea of the nearest–neighbor distance distribution of a stationary point process is to consider the distance distribution of a randomly chosen point to its nearest neighbor point. The numerical results obtained for this characteristic can be seen in Figure 4. They show that the model fits quite well to real data w.r.t. this structural characteristic, although not all values of the step function computed from real data are within the corresponding 96% confidence intervals computed from simulated data. Note that the appearance of the step function for real data results from the voxel–based representation by unions of spheres introduced in Section 3.

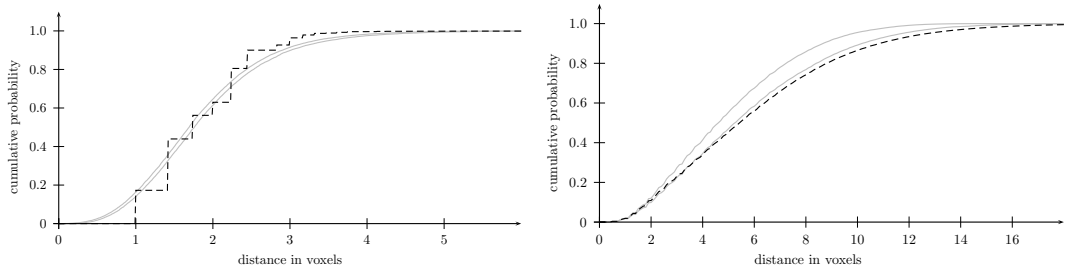

Figure 4: Cumulative distribution function of nearest–neighbor distances (left) and spherical contact distances (right) for real (black) and simulated (gray) data

A slightly different characteristic to analyze stationary point processes is the spherical contact distribution function. While for the nearest–neighbor distance distribution function the

distance from a randomly chosen point (of the point process) to its nearest neighbor point is considered, for the spherical contact distribution function the distance from an arbitrary point, not necessarily belonging to the point process, to the nearest point of the point process is considered. The numerical results obtained for this characteristic can be seen in Figure 4. Although the values computed for real data are not within the 96% confidence intervals, the values of the spherical contact distribution of the model are still quite close to those of real data.

Finally, we briefly discuss the pair-correlation function $g : (0, \infty) \to (0, \infty)$ which describes the frequency of point pairs with a given distance from each other, relative to the case of a stationary Poisson point process, see Appendix A. Recall that this characteristic has been used for model fitting. Thus, for a large range of $r > 0$, the values of $\widehat{g}(r)$ computed from real data should be within the corresponding 96% confidence intervals computed from simulated data. The numerical results can be seen in Figure 5.

The same should be true for the L-function of stationary point processes, because this function can be obtained from the g-function by integration and rescaling. Note that the L-function is a normalized version of the so–called K-function, i.e., for a stationary point process in $\mathbb{R}^d$ with intensity $\lambda > 0$ it holds that

$$L(r) = \sqrt[d]{\frac{K(r)}{b_d}},$$

where $K(r) = \int_0^r db_d s^{d-1} g(s) \mathrm{d}s$ and b_d denotes the volume of the d-dimensional unit sphere; see also Appendix A. In particular, for a stationary Poisson point process, i.e., a point process that follows the principle of complete spatial randomness, it holds that $L(r) = r$ for any $r > 0$. The results obtained for the L-functions computed from real and simulated data, respectively, can be seen in Figure 5.

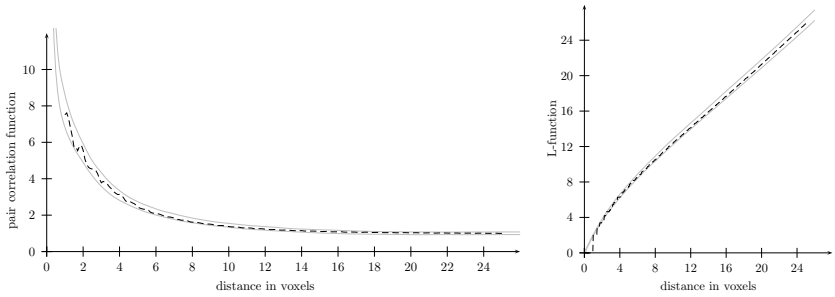

Figure 5: Pair–correlation function (left) and L-function (right) for real (black) and simulated (gray) data

4.2 Modeling of Grains

We now discuss the modeling of grains, i.e., the marks r_i being the radii of spheres with centers s_i, where our grain model is based on the idea of so–called geostatistical marking, i.e., conditioning on given realizations $\{s_i\}$ of the germ model $\{S_i\}$ described in Section 4.1.

4.2.1 Dependent Marking of Points

In the first step, the distribution of radii is estimated from real data, i.e., the empirical distribution of the radii in the sphere representation B''' of the pore phase has been computed. The results can be seen in Figure 6, where a shifted Γ-distribution $\Gamma(\rho, \zeta, \gamma)$ has been fitted with parameters $\rho = 2.26$, $\zeta = 2.85$, and the shift parameter $\gamma = \sqrt{3}$, i.e., the mean radius is 2.99. The fitting has been done using the maximum–likelihood method, which is described e.g. in Casella and Berger (2002).

A closer analysis of the radii shows that there exists a dependence structure which can be seen in Figure 7, displaying the mark–correlation function, where the values of this function describe the (empirical) correlation of pairs of radii in dependence of the distance between the corresponding pairs of centers. The results given in Figure 7 show that there is a strong

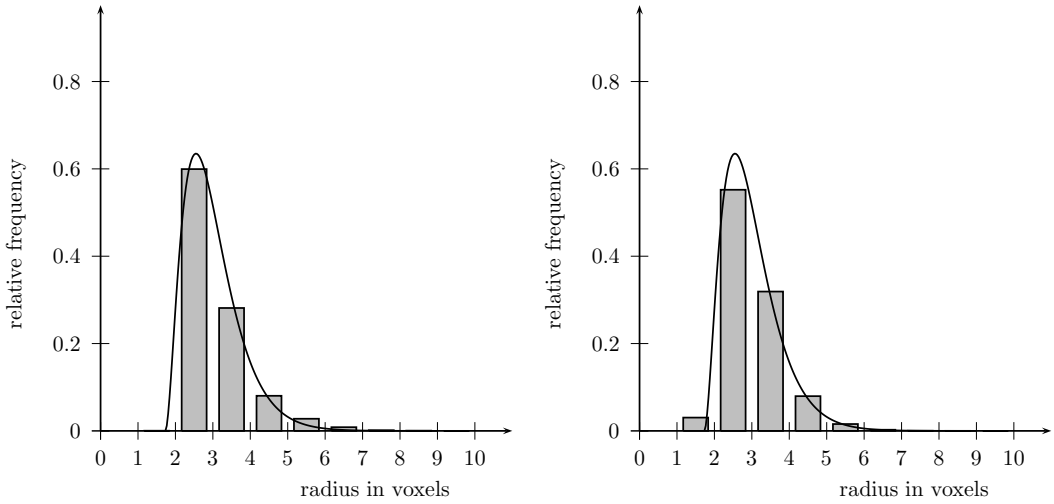

Figure 6: Histograms of radii with fitted Γ-distribution for real (left) and simulated (right) data

correlation of radii for pairs of centers being very close to each other, i.e., the marks of points being close together should be rather similar. On the other hand, the mark–correlation decreases to zero for pairs of points far away from each other. This indicates that such points can be marked independently. A formal definition of the mark–correlation function can be found e.g. in Illian *et al.* (2008).

To include the observed dependence structure into the model, we use a moving average procedure as described in Stenzel *et al.* (2010) and Thiedmann *et al.* (2010), where we proceed as follows. If there are, say, $n \geq 11$ points in the sampling window, we first associate these points with independent (unshifted) random variables $Z_1, \ldots, Z_n \sim \Gamma(\rho, \zeta/11, 0)$. Then, for the ith point of these n points, $i = 1, \ldots, n$, we consider its ten nearest neighbors with indices $i_1, \ldots, i_{10} \in \{1, \ldots, n\} \setminus \{i\}$, say. To construct the mark of the ith point, we consider the sum

$$Z_i + Z_{i_1} + \ldots + Z_{i_{10}} \sim \Gamma(\rho, \zeta, 0)\,.$$

Finally, we add the shift parameter γ and thus we achieve the required distribution $\Gamma(\rho, \zeta, \gamma)$

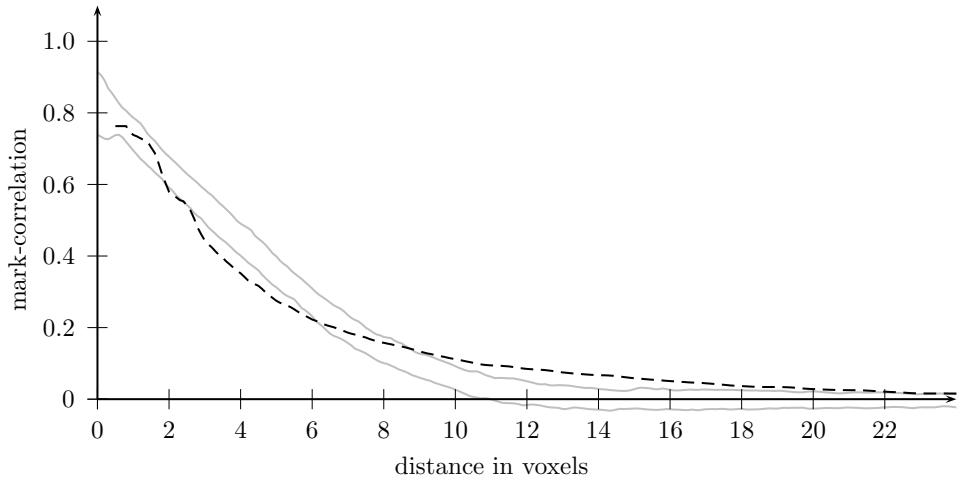

Figure 7: Mark–correlation function for real (black) and simulated (gray) data

of the marks $R_i = Z_i + \sum_{k=1}^{10} Z_{i_j} + \gamma$. The result is a marked point process $\{S_i, R_i\}$ with dependent marks following the required (shifted) Γ-distribution. But this marking does not yet meet the structure of the marks detectable in the sphere representation B''' well enough, where large spheres are predominantly located near the center of the pore phase and small spheres are preferred close to its boundaries (which results from the nature of the stochastic segmentation algorithm considered in Section 3). It turns out that the volume fraction of the unions of spheres simulated according to the rules described above is too large compared to the volume observed in real data, i.e., the volume of B'''. Hence an additional rearrangement of the marks is necessary which is described in the following section.

4.2.2 MCMC–Simulation to Rearrange Grains

To come closer to the results of the stochastic segmentation, i.e., the representation of the pore phase by unions of spheres considered in Section 3, we rearrange the marks representing the radii of spheres. The main focus lies on fitting the volume fraction of the model to the volume fraction of B''', i.e., the volume of the sphere representation of the pore phase. In

more detail, we consider a realization $\{s_i, r_i\}$ of the above described marked point process and interchange the marks r_i of the points s_i.

Recall that we have modeled the centers of spheres by a Matérn cluster process with elliptical clusters. We can assume that each cluster corresponds to a certain region of the pore phase. Hence we interchange only marks of points belonging to one and the same cluster. The cost function $f(s_1, r_{k_1}, \ldots, s_n, r_{k_n})$ which shall be minimized by interchanging the marks is given by

$$f(s_1, r_{k_1}, \ldots, s_n, r_{k_n}) = \left| |\bigcup_{i=1}^{n} b(s_i, r_{k_i})| - |B'''| \right|, \tag{4.1}$$

where $(k_1, \ldots, k_n)$ is some permutation of $(1, \ldots, n)$. This means that we fit the volume of the model to the volume of the sphere representation of real data. The interchange of marks can be implemented as follows. We choose a point at random among all points of the realized cluster process, say s_{i_1}. Then a second (different) point from the same cluster is chosen at random, say s_{i_2}, and the spheres $b(s_{i_1}, r_{i_2})$ and $b(s_{i_2}, r_{i_1})$ instead of $b(s_{i_1}, r_{i_1})$ and $b(s_{i_2}, r_{i_2})$ are considered. If the value of the cost function given in (4.1) decreases by interchanging the marks, the two marks are interchanged, otherwise not. This procedure is repeated until the relative difference between $|\bigcup_{i=1}^{n} b(s_i, r_{k_i})|$ and $|B'''|$ is smaller than 1%, say.

The result is a set of spheres where the volume of their union fits well to the volume of the sphere representation of the given data set. After this rearrangement, the mark–correlation function fits quite well to that of real data which can be seen in Figure 7.

4.3 Inversion of Morphological Smoothing

To the germ–grain model stated in Sections 4.1 and 4.2 we add a further modeling component in order to stochastically invert the morphological smoothing of the lithium–transporting phase described in Section 2.2, i.e., the opening and subsequent dilation of the set B.

4.3.1 Integration of Missing Connections

The investigation of connectivity before and after morphological smoothing shows that not only small pores in the solid phase, but also thin branches in the pore phase are removed which are important for the connectivity of the pore phase. This can also be seen from the changing degree of connectivity after the consecutive steps of image preprocessing (see Section 5.2.2 and Table 1). Hence we integrate the missing connectivity into the model by adding the removed pore volume at locations which are relevant for connectivity.

In a first step, we determine the volume which has to be added to the union of spheres, i.e., the pore volume that has been removed by the morphological smoothing. Hence, we determine the volume $|B \setminus B''|$ of the set difference $B \setminus B''$. It turns out that this volume is smaller than 0.6 % of the total volume of the sampling window, where the small isolated pores removed by morphological smoothing have a total volume smaller than 0.1 % and the thin branches, i.e., the parts connected to the main pore phase, of about 0.5 %. Thus, we only integrate the missing thin branches into the germ–grain model. This seems to be reasonable because the small isolated parts of the pore phase have no essential influence on the performance of Li-ion batteries.

Furthermore, we assume that all parts which have to be added to the germ–grain model developed in Sections 4.1 and 4.2 can be seen as spheres with radius $r = \sqrt{3}$. This assumption is motivated by the fact that a spherical structuring element with radius $\sqrt{3}$ has been used for the opening of pore phase considered in Section 2.2, i.e., the diameter of the removed parts is smaller or equal $2\sqrt{3}$.

To compensate the effects of this opening, which essentially influences the connectivity of the pore phase, we choose the following model to improve connectivity. For integrating the missing connections we consider a Coxian point process $\{S_i'\}$, which is also called a doubly–

stochastic Poisson point process in the literature, with preferred locations of points between non-connected clusters of spheres $b(S_i, R_{k_i})$. In particular, for any realization $\{s_i, r_{k_i}\}$ of the germ–grain model $\{S_i, R_{k_i}\}$ as described in Sections 4.1 and 4.2, we assume that $\{S_i'\}$ is a (conditional) inhomogeneous Poisson point process, where the intensity field $\{\lambda(x), x \in \mathbb{R}^3\}$ of this Poisson process depends on the union of spheres $\xi = \bigcup_{i=1}^{\infty} b(s_i, r_{k_i})$. Let the clusters of spheres in the set ξ be denoted by $C_1, C_2, \ldots$, i.e., $\xi = \bigcup_{i=1}^{\infty} C_i$ where $C_i \cap C_j = \emptyset$ for $i \neq j$. Due to the fact that the missing volume of the pore phase has to be placed in between these clusters to increase the degree of connectivity, we put

$$\lambda(x) = \begin{cases} \lambda_b & \text{if } x \in \mathbb{R}^3 \setminus \xi \text{ and } c(x) \geq 2, \\ 0 & \text{otherwise}, \end{cases} \tag{4.2}$$

where $\lambda_b > 0$ is some constant and $c(x)$ denotes the number of clusters C_i of ξ hitting the sphere $b(x, 1/2 + \sqrt{3})$, i.e., $c(x) = \#\{i : b(x, 1/2 + \sqrt{3}) \cap C_i \neq \emptyset\}$. For any realization $\{s_i'\}$ of the (conditional) Poisson process $\{S_i'\}$ with this intensity field $\{\lambda(x), x \in \mathbb{R}^3\}$, the union of spheres $\bigcup_{i=1}^{\infty} b(s_i', \sqrt{3} + 1)$ with deterministic radius equal to $r = \sqrt{3} + 1$ is added to the set ξ. Then, by

$$\xi' = \bigcup_{i=1}^{\infty} b(s_i, r_{k_i}) \cup \bigcup_{i=1}^{\infty} b(s_i', \sqrt{3} + 1)$$

a realization of the model after adding the connecting spheres $b(s_i', \sqrt{3} + 1)$ is given. Note that the radius $r = \sqrt{3}$ used for the opening described in Section 2.2 is increased by 1 because subsequently (see Section 4.3.2) further morphological operations are applied which should not remove the spheres $b(s_i', \sqrt{3})$.

To compute the constant λ_b appearing in (4.2), we temporarily assume that the spheres $b(s_i', \sqrt{3})$ do not overlap and that each of these spheres contributes with its total volume to increasing the volume of ξ. Under these simplifying assumptions, λ_b can be estimated by

$$\widehat{\lambda}_b = \frac{0.005 \cdot |W|}{|b(o, \sqrt{3})| \cdot |\{x : x \in W \setminus \xi, c(x) \geq 2\}|},$$

where 0.005 is the (total) volume fraction of the thin branches to be added to the set ξ. Using this formula, we obtained the average value $\widehat{\lambda}_b = 0.12$ from repeated simulations of the germ–grain model $\{S_i, R_{k_i}\}$ as described in Sections 4.1 and 4.2. At first glance, this relatively high value of the (conditional) intensity λ_b of sphere centers $\{S_i'\}$ seems to contradict the assumption that the corresponding spheres do not overlap. But, the set $\{x : x \in W \setminus \xi, c(x) \geq 2\}$, where these spheres are put, consists of a large number of thin 'sheets', which are rather small and well-separated from each other. This makes the assumption of non–overlapping reasonable. Furthermore, we include the spheres $b(s_i', \sqrt{3}+1)$ with 'dilated' radius $\sqrt{3}+1$, instead of $\sqrt{3}$, to ensure that the morphological operations described in Section 4.3.2 do not destroy the included connections between the clusters C_i of the set ξ. This additionally increases the included volume and compensates occasional overlappings of the spheres $b(s_i', \sqrt{3}+1)$.

4.3.2 Inversion of Dilation

The aim of the following modeling component is to compensate the dilation of the (opened) pore phase B' considered in Section 2.2. Simultaneously, some small gaps within the set ξ' are eliminated which are modeling artifacts resulting from the representation of pore phase by unions of spheres.

Thus, we first open the complement $\mathbb{R}^3 \setminus \xi'$ of the set ξ' to remove these gaps, using the sphere $b(o,1)$ as structuring element. The corresponding realization of our model after this morphological operation is denoted by ξ''. Then, we stochastically invert the dilation of the pore phase considered in Section 2.2, i.e., we dilate the complement $\mathbb{R}^3 \setminus \xi''$ of the set ξ'' obtained in the previous step, where we use the same structuring element $b(o,1)$ as for the dilation of B' considered in Section 2.2. Finally, the realization of the complete model is denoted by ξ'''. A 3D image showing a cutout of such a realization of our stochastic simulation

model for the pore phase is given in Figure 1 (right).

5 Model Validation

To validate the stochastic simulation model for the pore phase developed in Section 4, we compare structural image characteristics of real and simulated data which are especially relevant w.r.t. transport properties of Li-ion batteries. These characteristics have been computed for the real (binarized) 3D data and for 100 realizations of our model.

5.1 Graph Representation of Pore Phase

Most of these characteristics are based on a graph representation of the pore phase. To obtain such a representation, we consider a voxel–based representation of the original binarized data and of the realizations of our model, respectively. Then, in a first step, the pore phase is skeletonized, where some voxels belonging to the pore phase are changed into 'solid voxels' in a way that the remaining voxel–based lines representing the pore phase have a thickness of one voxel. Note that this transformation does not change the connectivity of the pore phase. In the next step, the voxel–based lines are transformed into vector data, i.e., voxel–based line segments are replaced by (vector–based) line segments or polygonal tracks, respectively. A detailed description of the applied algorithms can be found in Fourard *et al.* (2006); another recent application of these skeletonization algorithms to the analysis of complex pore systems is described in Thiedmann *et al.* (2009).

5.2 Results

The results obtained for the structural image characteristics considered in this section are presented in various figures. For cumulative probability distribution functions of these char-

acteristics, (pointwise) 96% confidence intervals computed from simulated data are plotted in gray and the values obtained for real data are plotted as dashed black lines. These graphical representations indicate whether the real data can be seen as a realization of the stochastic simulation model developed in Section 4. If probability densities are considered, histograms are plotted. Additional to the plots, results obtained for mean values and standard deviations are given in Tables 1 and 2.

5.2.1 Porosity

The first and most important characteristic of porous material is its porosity, i.e., the volume fraction of the pore phase. As can be seen in the first and last columns of Table 1, with respect to this characteristic the model fits quite well to real data.

5.2.2 Connectivity

Another fundamental characteristic of porous material is its connectivity, because diffusion processes can only take place in the pore phase if this phase is sufficiently well connected. Hence we have computed the connectivity of the pore phase from top to bottom and vice versa. Therefore we consider the voxel–based representation of the 3D morphology and compute the connected volume fractions of the pore phase where we apply the same methods as in Oosterhout *et al.* (2009). The results shown in the first and last columns of Table 1 coincide nicely for real and simulated data.

5.2.3 Specific Interior Surface Area

Chemical reactions take place at the interface between pore and solid phase and their reaction rates are proportional to the size of this interface. Hence a very important structural

	real data			simulated data			
	B	B''	B'''	ξ	ξ'	ξ''	ξ'''
connectivity							
top to bottom	0.966	0.930	0.937	0.901	0.966	0.989	0.967
bottom to top	0.964	0.914	0.923	0.904	0.966	0.989	0.967
porosity	0.166	0.215	0.224	0.231	0.239	0.250	0.166

Table 1: Connectivity and porosity of pore phase for real and simulated data

characteristic related to performance of Li-ion batteries is the specific interior surface area, i.e., the mean surface area of the (interior) pore space per unit volume. The results of 0.079 and 0.085 obtained for real and simulated data, respectively, are rather similar to each other, i.e., the model fits quite well to real data w.r.t. this characteristic.

5.2.4 Geometric Tortuosity

For a more detailed description of transport and diffusion processes in porous materials, the tortuosity of the pore phase can be considered. This characteristic is usually defined as the ratio of the mean effective path length through a material and the material thickness. However, we consider a slightly modified structural characteristic, where we consider shortest path lengths instead of effective path lengths, which leads to the notion of geometric tortuosity. Hence, we proceed like in Thiedmann *et al.* (2009) extracting a graph from the pore space, see Section 5.1, and running the computations along the edges of the graph.

We are aware that the purely structural definition of tortuosity considered above does not coincide with the tortuosity factor usually used to describe transportation processes in Li-ion batteries, see also the discussion in Shearing *et al.* (2010), where a similar structural characteristic is considered. However, for validating our model of Li-ion batteries, the notion

of geometric tortuosity is very useful.

The advantage of the shortest–path approach is that not only a mean value but a complete probability distribution of geometric tortuosity can be computed, which contains much more information. The results presented in Figure 8 show that the histograms computed for real and simulated data are similar, though not identical, where the histogram of geometrical tortuosity obtained from simulated data is a bit broader and slightly shifted to the right, see also Table 2.

	real data		simulated data	
	mean	sd	mean	sd
tortuosity	1.59	0.22	1.82	0.29
object based pore size	3.12	1.32	3.09	1.15
coordination number	2.73	1.27	2.71	1.16
spherical contact distribution	1.83	0.99	1.70	0.84

Table 2: Means and standard deviations for real and simulated data

A possible explanation for these differences between the histograms in Figure 8 could be that our model produces images with pore phases which perhaps are a bit too diffuse, i.e. not enough clustered (see also Figure 1), and that this could be the reason for a slightly too large mean and variance of shortest path lengths generated by our simulation model. This seems to be in accordance with the situation visualized in Figure 4 for cumulative probability distribution functions of spherical contact distances, see also Figure 12 below. These two figures show that spherical contact distances observed in real battery data possess a tendency to be a bit longer than the corresponding spherical contact distances computed from simulated data.

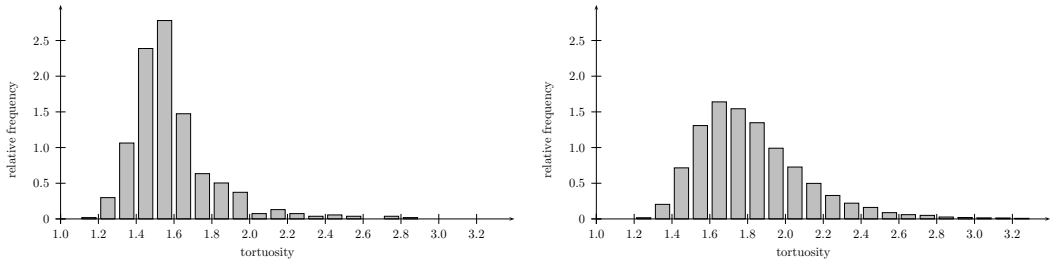

Figure 8: Distribution of geometric tortuosity of real (left) and simulated (right) data

5.2.5 Pore Size Distributions

Another important characteristic for describing transport processes is the pore size distribution. However, no unique rule is given in the literature for computing this characteristic from 3D images, wherefore we apply two different kinds of pore size distributions, following Thiedmann *et al.* (2010) and Münch and Holzer (2008), respectively.

The first one is based on a graph representation of the pore phase, where all nodes of the graph are considered as potential pore centers. The shape of the pores is assumed to be spherical, i.e., we compute for each potential pore center the largest radius of a sphere around it that is still fully contained in the pore phase. This set of (potential) pores is subsequently thinned in such a way that no pore center is contained in another (larger) pore. For the remaining set of pores, the pore size distribution is determined. The results shown in Figure 9 coincide quite nicely for real and simulated data, see also Table 2.

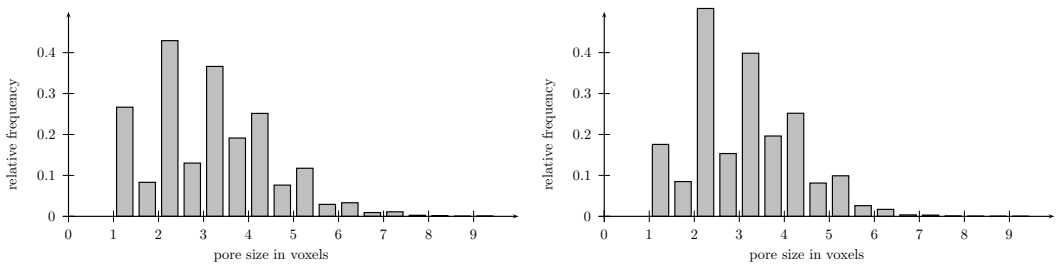

Figure 9: Object-based pore size distributions of real (left) and simulated (right) data

In contrast to this object–based definition of pores and their sizes, a completely different

notion of pore sizes has been considered in Münch and Holzer (2008) which is based on volume fractions. The idea is to determine the volume fraction of the pore phase that can be covered by spheres with a given radius. More precisely, to determine the value of this pore size distribution at r, the volume fraction of the pore phase that can be covered by spheres with radius r is determined. It is obvious that this volume fraction increases for decreasing radii r.

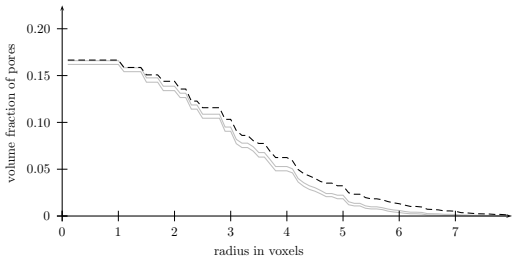

Figure 10: Pore size distributions based on volume fractions, for real (black) and simulated (gray) data

The results obtained w.r.t. this image characteristic for real and simulated data, respectively, can be seen in Figure 10. Similar to the effect mentioned in Section 5.2.4 regarding spherical contact distances, the pore sizes of this type observed in real data are sligthly larger than those computed from simulated data. Note that the latter notion of pore sizes has been considered also in Shearing *et al.* (2010) to characterize microstructures of Li-ion batteries.

5.2.6 Coordination Number

In the previous section, a definition of pores and their sizes based on a graph representation of the pore phase has been introduced. But not only volume-orientated properties of this representation of the pore phase are important for characterizing the microstructure of porous media, but also connectivity properties of the graph are of interest, especially in the context of transport processes. A basic characteristic to describe the connectivity of graphs is the

distribution of their coordination number, i.e., the number of necks or throats emanating from a pore.

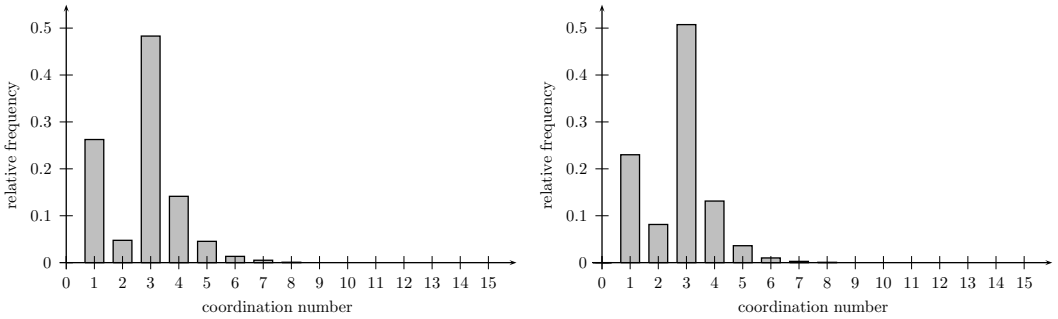

Figure 11: Distribution of coordination number for real (left) and simulated (right) data

This tool is frequently used in geology (Blunt *et al.* (2002)). It can be computed quite easily using the graph representation of the pore phase and the object–based definition of pores mentioned in Section 5.2.5. We just have to count the numbers of edges of the graph emanating from each pore. The results obtained for real and simulated data coincide quite nicely. They are shown in Figure 11, see also Table 2.

5.2.7 Minimum Spanning Tree

Another characteristic describing the connectivity of graphs is the so-called minimum spanning tree (MST), a popular tool in graph theory (Diestel (2005), Jungnickel (1999)). The idea is to consider the sub–graph with the minimum length but the same connectivity as the original graph, i.e., all nodes that are connected in the original graph are still connected in the MST. As a quantitative characteristic to describe connectivity, we consider the relative length ℓ of the MST, i.e.,

$$\ell = \frac{\text{length of the MST}}{\text{length of the original graph}},$$

where we obtained the value $\ell = 0.56$ for both real and simulated data.

5.2.8 Spherical Contact Distribution Function

In most of the previous sections, we have considered properties based on the graph representation of the pore phase introduced in Section 5.1. However, the spherical contact distribution function of the pore phase is not based on this graph representation. It is closely related to the voxel–based notion of pore size distribution discussed in Section 5.2.5. Its basic idea is to consider the distribution of the shortest distance at a randomly chosen point of the pore phase to the solid phase, and vice versa. The results obtained w.r.t. this characteristic for real and simulated data are shown in Figure 12, see also Table 2. As already mentioned earlier, the shortest distances from pore phase to solid phase observed in real data are a bit longer than those computed from simulated data.

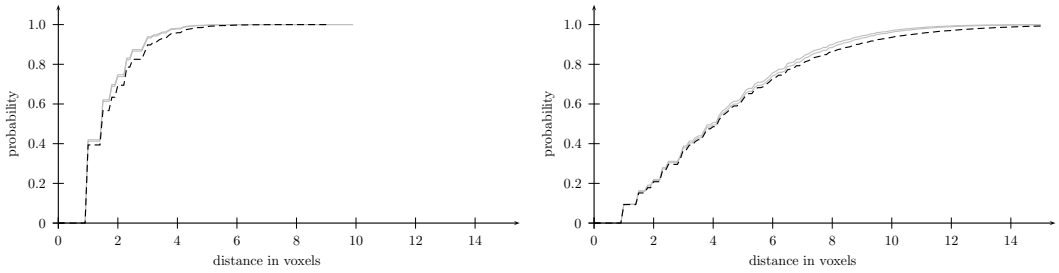

Figure 12: Spherical contact distribution functions for real (black) and simulated (gray) data; left: from pore phase to solid phase; right: from solid to pore phase

6 Summary and Conclusions

In this paper, we have developed, fitted, and validated a stochastic simulation model for the 3D microstructure of composite materials used in Li-ion batteries which is based on tools from stochastic geometry and spatial statistics. Therefore, following Shearing *et al.* (2010), we consider the Li–transporting phase as pores and the graphite as solid. The microstructure of the pore phase is of essential importance for the lithium–transport processes within batteries,

because their efficiency and performance depend on suitable transportation pathways with optimal shapes.

For modeling and especially for fitting our model to real data, the 3D data set described and analyzed in Shearing *et al.* (2010) has been considered.

In a first step, we have applied a preprocessing of image data, where we have smoothed the binarized image using several morphological transformations. Note that the details of the image, removed by this smoothing, are not neglected but included into the model as one of the modeling components.

For modeling the pore phase by appropriate tools from stochastic geometry, we transform the smoothed pore phase into an off-grid representation by unions of overlapping spheres, where we proceed in a similar way as suggested in Stenzel *et al.* (2010). To get a suitable representation of this type, we use a stochastic segmentation technique, i.e., we describe the pore phase as a realization of a random marked point process, where the points are the centers of spheres and the marks are the corresponding radii.

The stochastic model for these unions of spheres is built in two steps. First, the centers are modeled by a 3D Matérn cluster process with elliptically shaped clusters. Then, given a realization of this point–process model, the radii are modeled as marks of these points, where the radii are generated by means of a moving–average procedure and a subsequent MCMC-simulation for rearrangements. Finally, the image details removed by morphological smoothing are integrated into the model, where a (Coxian) point process is considered, combined with several morphological operations, in order to integrate missing connections of the pore phase and to stochastically invert the morphological smoothing.

The complete model constructed in this way is then validated by means of global image characteristics which describe transport–relevant properties of the pore phase. In numerous

figures and tables the values obtained for these characteristics from real and simulated data, respectively, are given. They show that the model fits quite well to real data.

In future research, we will use our model in order to generate virtual microstructures of Li-ion batteries which serve as an input for virtual scenario analyses. In particular, the lithium–transport properties of these virtual structures will be analyzed by numerical transport models to come up with a complete mathematical description of the relationships between structural and transportation properties of Li-ion batteries. Then, using such a combination of mathematical models and methods, optimal microstructures of the pore phase can be detected which are preferable for highly efficient Li-ion batteries. Hence, in a first step, the understanding of various structural and transportation processes within existing Li-ion batteries can be improved, and, in a second step, virtual morphologies with improved physical properties can be generated and analyzed on the computer with the aim to construct/engineer such improved materials in real labs.

A Formulae for the Pair–Correlation Function

One possibility to fit a point–process model to real data is the method of minimum–contrast estimators. The idea for this fitting technique is the minimization of the distance between a characteristic of the point–process model and the values of this characteristic estimated from real data. In Section 4.1.2, we have chosen the pair–correlation function for fitting a point-process model to real data, because this second-order characteristic contains comprehensive structural information. In the following, a short description of this characteristic is given. Further details can be found e.g. in Illian *et al.* (2008), Stoyan *et al.* (1995).

For a stationary point process $\{S_i\}$ with intensity $\lambda > 0$, where λ is the mean number of

points per unit volume, the so–called K-function is given by

$$K(r) = \mathbb{E}_0(\#\{S_i, |S_i| < r\} - 1)/\lambda\,, \quad r \geq 0\,,$$

where the symbol $\mathbb{E}_0$ means conditional expectation under the condition that there is a point of $\{S_i\}$ located at the origin. In other words, the value of the K-function at r describes the mean number of points in a sphere with radius r around the 'typical', i.e., 'randomly chosen', point of $\{S_i\}$ without counting the point itself. Using this definition of the K-function, the pair-correlation function (or g-function) of a stationary point process in $\mathbb{R}^d$ can be given by

$$g(r) = \frac{\frac{\mathrm{d}}{\mathrm{d}r}K(r)}{db_d r^{d-1}}\,, \quad r \geq 0\,,$$

where b_d denotes the volume of the unit sphere in $\mathbb{R}^d$. The g-function can be interpreted as follows. For $r > 0$ such that $g(r) > 1$, there are more point pairs with distance r to each other compared to a Poisson point process with the same intensity λ. Vice versa if $g(r)$ is smaller than 1, this means there are less point pairs with such a distance compared to a Poisson point process with the intensity. If $g(r) = 0$, then there are no point pairs with distance r.

For Matérn cluster point processes in $\mathbb{R}^3$ with elliptically shaped clusters, the pair–correlation function depends on the parameter vector $\theta = (\lambda_p, l_1, l_3)$ and is given by

$$g_\theta(r) = 1 + \frac{f_{l_1/2, l_3/2}(r)}{4\pi\lambda_p r^2}\,,$$

where $f_{l_1/2,l_3/2}(r)$ denotes the density of the distance distribution between two randomly chosen points within one cluster. In the following, we will denote the radii of the elliptical cluster regions by $(r_1, r_1, r_3) = (l_1/2, l_1/2, l_3/2)$. Recall that we assume that $l_1 = l_2$ holds.

Furthermore, note that

$$f_{r_1,r_3}(r) = \frac{f_{\mu,1}(\frac{r}{r_3})}{r_3}\,, \quad r \geq 0\,,$$

where $\mu = r_1/r_3$ and $f_{\mu,1}(r)$ denotes the density of the distance distribution of two randomly chosen points in a spheroid with two semiaxes of length μ and the third of length one. The

following formulae can be found in García-Pelayo (2005). It holds that

$$f_{\mu,1}(r) = \int_0^1 \frac{1}{\sqrt{\mu^2(1-x^2)+x^2}} f_{1,1}\left(\frac{r}{\sqrt{\mu^2(1-x^2)+x^2}}\right) \mathrm{d}x\,, \qquad r \geq 0\,,$$

where $f_{1,1}(r)$ is the density of the distance distribution of two randomly chosen points within the unit sphere, which is given by

$$f_{1,1}(r) = \begin{cases} \frac{3}{16}(r-2)^2 r^2 (r+4) & \text{if} \quad 0 < r < 2\,, \\ 0 & \text{otherwise}\,. \end{cases}$$

If $\mu \geq 1$, i.e., $r_1 \geq r_3$, the integral can be computed analytically and it holds that

$$f_{\mu,1}(r) = \begin{cases} 12b^2 - 9\left(\mu + \frac{\ln\left(\mu+\sqrt{\mu^2-1}\right)}{\sqrt{\mu^2-1}}\right) b^3 & \\ \quad + \frac{3}{4}\left(\mu(3+2\mu^2) + 3\frac{\ln\left(\mu+\sqrt{\mu^2-1}\right)}{\sqrt{\mu^2-1}}\right) b^5 & \text{if} \quad 0 < r \leq 2\,, \\ \frac{9\sqrt{b}}{4\sqrt{\mu^2-1}}\left(\sqrt{1-b}(2+b) + b(b-4)\ln\left(\frac{1+\sqrt{1-b}}{\sqrt{b}}\right)\right) & \text{if} \quad 2 < r \leq 2\mu\,, \\ 0 & \text{otherwise}\,. \end{cases}$$

where $b = \left(\frac{r}{2\mu}\right)^2$.

If $\mu < 1$, we use the Gauss–Legendre method with 5 supporting points to approximate the value of the integral, see e.g. Stoer and Bulirsch (1996).

References

Verbrugge M. and Koch B. (2003) Electrochemical analysis of lithiated graphite anodes. *Journal of the Electrochemical Society*, **150**, A374–A384.

Shearing P.R., Howard L.E., Jørgensen P.S., Brandon N.P., and Harris S.J. (2010) Characterization of the 3-dimensional microstructure of a graphite negative electrode from a Li-ion battery. *Electrochemistry Communications*, **12**, 374–377.

Wilson J.R., Cronin J.S., Barnett S.A., and Harris S.J. (2010) Measurement of three-dimensional microstructure in a LiCoO2 positive electrode. *Journal of Power Sources (in press).*

Stenzel O., Hassfeld H., Thiedmann R., Koster L.J.A., Oosterhout S.D., van Bavel S.S., Loos J., Wienk M.M., Janssen R.A.J., and Schmidt V. (2010) Spatial modelling of the 3D morphology of hybrid polymer-ZnO solar cells, based on electron tomography data. *Preprint (submitted).*

Yi Y.B., Wang C.W. and Sastry A.M. (2004) Two–dimensional vs. three-dimensional clustering and percolation in fields of overlapping ellipsoids. *Journal of the Electrochemical Society*, **151**, A1292-A1300.

Yi Y.B., Wang C.W. and Sastry A.M. (2006) Compression of packed particulate systems: Simulations and experiments in graphitic li-ion anodes. *Journal of Engineering Materials and Technology*, **128**, 73-80.

Kendall W.S. and Molchanov I. (eds.) (2010) *New Perspectives in Stochastic Geometry.* Springer, Berlin.

Gelfand A.E., Diggle P.J., Fuentes M., and Guttorp P. (eds.) (2010) *Handbook of Spatial Statistics.* CRC Press, Boca Raton.

Harris S.J., Deshpande R.D., Qi Y., Dutta I., and Cheng Y.T. (2010) Mesopores inside electrode particles can change the Li-ion transport mechanism and diffusion-induced stress. *Journal of Materials Research*, **25**, 1433–1440.

Jähne B. (2005) *Digital Image Processing.* 6th revised and extended ed., Springer, Berlin.

Weikert J. (1998) *Anisotropic Diffusion in Image Processing.* Teubner, Stuttgart.

Saito T. and Toriwaki J.-I. (1994) New algorithms for euclidean distance transformations of an n-dimensional digitized picture with applications. *Pattern Recognition*, **27**, 1551–1565.

Scott D.W. (1992) *Multivariate Density Estimation: Theory, Practice, and Visualization.* J. Wiley & Sons, New York.

Daley D.J. and Vere-Jones D. (2003) *An Introduction to the Theory of Point Processes, Volumes I and II.* Springer, New York.

Diggle P.J. (2003) *Statistical Analysis of Spatial Point Patterns.* Arnold, London.

Illian J., Penttinen A., Stoyan H., and Stoyan D. (2008) *Statistical Analysis and Modelling of Spatial Point Patterns.* J. Wiley & Sons, Chichester.

Stoyan D., Kendall W.S., and Mecke J. (1995) *Stochastic Geometry and its Applications.* 2nd ed. J. Wiley & Sons, Chichester.

Casella G. and Berger R. L. (2002) *Statistical Inference.* 2nd ed. Duxbury, Pacific Grove (CA).

Thiedmann R., Schmidt V., Manke I., and Lehnert W. (2010) Random geometric graphs for modelling the pore space of fibre-based materials. *Preprint (submitted).*

Fourard C., Malandain G., Prohaska S., and Westerhoff M.(2006) Blockwise processing applied to brain microvascular network study. *IEEE Transactions on Medical Imaging*, **25**, 1319–1328.

Thiedmann R., Hartnig C., Manke I., Schmidt V., and Lehnert W. (2009) Local structural characteristics of pore space in GDL's of PEM fuel cells based on geometric 3D graphs. *Journal of the Electrochemical Society*, **156**, B1339-B1347.

Oosterhout S. D., Wienk M. M., van Bavel S. S., Thiedmann R., Koster L. J. A., Gilot J., Loos J., Schmidt V., and Janssen R. A. J. (2009) The role of three-dimensional morphology on the efficiency of hybrid polymer solar cells. *Nature Materials*, **8**, 818-824.

Münch B. and Holzer L. (2008) Contradicting geometrical concepts in pore size analysis attained with electron microscopy and mercury intrusion. *Journal of the American Ceramic Society*, **91**, 4059–4067.

Blunt M.J., Jackson M.D., Piri M., and Valvatne P.H. (2002) Detailed physics, predictive capabilities and macroscopic consequences for pore–network models of multiphase flow. *Advances in Water Resources*, **25**, 1069–1089.

Diestel R. (2005) *Graph Theory*. Springer, Heidelberg.

Jungnickel D. (1999) *Graphs, Networks and Algorithms*. Springer, Berlin.

García-Pelayo R. (2005) Distribution of distance in the spheroid. *Journal of Physics A: Mathematical and General*, **38**, 3475 - 3482.

Stoer J. and Bulirsch R. (1996) *Introduction to Numerical Analysis*. 2nd ed. Springer, New York.